Journal of
Materials Chemistry C

PAPER

View Article Online
View Journal | View Issue

Cite this: J. Mater. Chem. C, 2019, 7, 4382

Impact of structural anisotropy on electro-mechanical response in crystalline organic semiconductors†

Sai Manoj Gali, *[ab] Claudio Quarti, [a] Yoann Olivier, [a] Jérôme Cornil, [a] Lionel Truflandier,[b] Frédéric Castet, [b] Luca Muccioli *[bc] and David Beljonne *[a]

Received 18th December 2018,
Accepted 5th March 2019

DOI: 10.1039/c8tc06385k

rsc.li/materials-c

In an effort to gain a fundamental understanding of the electromechanical response in high mobility crystalline organic semiconductors, we have investigated the uniaxial strain–mobility relationships in rubrene and benzothienobenzothiophene crystals. Elastic moduli and Poisson ratios of the materials are evaluated and the strain mobility response of these materials is rationalized using the effective masses and electronic couplings in the framework of hopping and band transport models, giving consistent results. The microscopic origin of the response is investigated in relation to the strain induced variations in the inter- and intra-molecular degrees of freedom. We demonstrate that the strain applied along one of the crystallographic directions in these materials does not only induce mobility variations along the same direction, but also along the other crystallographic directions that are mechanically coupled with large Poisson ratios. A rational design of electronic devices could therefore benefit from the efficient exploitation of this anisotropic strain mobility response in relation to the inherent crystalline anisotropy.

1 Introduction

Owing to their ease of synthesis, low cost of production and good responsiveness, opto-electronic devices based on organic semiconductors have entered into the mainstream of commercialized products with applications ranging from organic light emitting devices (OLEDs), organic photovoltaics (OPVs), and organic field effect transistors (OTFTs) to biocompatible organic electronic devices.[1,2] Indeed, the flexible nature of organic materials[3–5] has prompted the development of cutting edge diagnostic devices interfaced with the human body,[6,7] such as bio-integrated circuits[7] or artificial skins.[8]

Of late, micro electro mechanical systems (MEMs) based on organic semiconductor single crystals have also gained scientific attention. In a seminal study, Briseno *et al.* demonstrated that the performances of rubrene-based field effect transistors (FETs) could be improved upon flexing.[9] These investigations were later extended by applying local strains of different magnitudes along the conducting channel of rubrene FETs (corresponding to the π-stacking direction within the crystal), which demonstrated that the charge carrier mobility increases upon application of a compressive strain, whereas it diminishes when applying a tensile strain.[10] Complementary to these works, studies by Batlogg *et al.*[11] showed an increase of mobility in rubrene FETs for compressive strains applied either along the crystalline axis parallel to the π-stacking direction or along the axis parallel to the herringbone packing.

On similar grounds, by combining experimental measurements and theoretical calculations, some of us demonstrated that the strain-induced variation of charge-carrier mobility in rubrene single crystals originates from the variation of electronic couplings between molecular neighbours, and that the anisotropy of the rubrene crystal structure induces an anisotropy in its strain response.[12] Importantly, this study evidenced that applying a mechanical strain along a given crystalline direction does not only change the intermolecular distance parallel to that direction, but induces more global variations in both intra- and intermolecular degrees of freedom, making transfer integral variations not straightforward to rationalize. These complex relationships between mechanical strain and charge transport efficiency in organic FETs have been illustrated in several studies, leading to seemingly contradictory observations. In some materials, application of a compressive strain increases the charge carrier mobility,[13–16] whereas in others, the mobility

[a] Laboratory for Chemistry of Novel Materials, University of Mons, 7000-Mons, Belgium. E-mail: saimanoj.gali@umons.ac.be, david.beljonne@umons.ac.be
[b] Institut des Sciences Moléculaires, UMR 5233, University of Bordeaux, 33405-Bordeaux, France
[c] Dipartimento di Chimica Industriale "Toso Montanari", University of Bologna, 40100-Bologna, Italy. E-mail: luca.muccioli@unibo.it

† Electronic supplementary information (ESI) available. See DOI: 10.1039/c8tc06385k

diminishes[17–20] or does not display any sizeable variation. For instance, strain–mobility in TIPS-pentacene does not change upon bending[21,22] but is modified when applying shear[23] or lateral deformation.[19,24] To further complicate the picture, previous studies evidenced that the strain–mobility responses can be influenced by the substrate underneath the organic semiconductor owing to the mechanical and thermal expansion inhomogeneities[13,25–27] and can also be influenced by the modulation of charge injection at the semiconductor–electrode interface.[28]

The rational design of mechanically-responsive electronic devices thus requires a fundamental understanding of the relationships linking the transfer integral variations to the changes in intra/intermolecular degrees of freedom induced by directional mechanical strains. In this regard, the present work reports a theoretical investigation of the strain–mobility response of different high-mobility crystalline organic semiconductors, namely three rubrene polymorphs (orthorhombic, RO, triclinic, RT, and monoclinic, RM) as well as three [1]benzothieno[3,2-*b*][1]benzothiophene (BTBT) derivatives, unsubstituted (B0) and with either octyl (B8) or dodecyl chains (B12) attached at the 2,7 positions. The strain–mobility responses are rationalized within the two limit regimes for hole transport, namely hopping and band transport, in terms of transfer integral and effective mass variations with respect to directional mechanical strain, respectively. In addition, we also provide the elastic moduli of the investigated materials, along with the Poisson ratios that are indicative of the mechanical coupling between the different crystallographic axes.

2 Computational details

Plane-wave (PW) density functional theory (DFT) calculations were performed using the Quantum Espresso (QE) software.[29] As intermolecular interactions in organic semiconductor crystals are dominated by the van der Waals forces, explicit introduction of vdW interactions in the exchange–correlation kernel has been considered for all the QE-PW-DFT calculations.[30–32] The choice of the C09 van der Waals density functional (c09-vdW-DF) proposed by Cooper[33] was motivated by its overall good performance in reproducing weak bonding situations in a broad set of systems, including molecular dimers and layered bulk systems.[34,35] Geometry relaxations, including atomic positions and cell parameters, were performed starting from the experimental crystallographic structures, as reported in Table 1, employing a regular *k*-point spacing of about 0.4 $Å^{-1}$. The kinetic energy and charge density cutoffs were set to 50 Ry (~680 eV) and 350 Ry (~4760 eV), respectively. Force and stress were minimized with thresholds of 5×10^{-4} a.u. and 0.3×10^{-4} a.u. (0.2 kbar), respectively.

Uniaxial compressive and tensile strains were then applied along the three crystallographic axes of the optimized structures, up to ±0.8% of normal strain, $\varepsilon_i = (L_i - L_{i,0})/L_{i,0}$ with increments of ±0.2%, where $L_{i,0}$ and L_i are the unstrained and strained lengths of the crystal cell along the direction *i*. Uniaxial strain implies that homogeneous strain was imposed by simultaneously rescaling one of the crystal cell dimensions and the molecular positions along the same direction, and for every strain value (compressive and tensile), the relative lattice vectors were held fixed while all internal degrees of freedom (atomic positions) were relaxed self-consistently. Subsequently, geometries optimized with and without external strain were used to compute the hole transfer integral (J) for all neighbouring molecular pairs within the crystal, by employing the projection method[36] at the PBE/DZ level using the Amsterdam Density Functional (ADF) package.[37] Finally, band structure calculations were performed at the vdw-DF-C09 level along the high symmetry paths of the respective crystals (see the ESI,† for details). The hole effective mass (m) was computed from the dispersion of the valence band energy E,[38] using the expression:

$$\frac{\hbar^2}{m} = \frac{\delta^2 E(\mathbf{k})}{\delta \mathbf{k}^2} \quad (1)$$

In practice, a second order polynomial was fitted to the band, in the region of reciprocal space going from the Γ-point to the

Table 1 Experimental and calculated (DFT, from this work) crystallographic parameters for rubrene polymorphs and BTBT derivatives. Space Group (SG) is represented in Hermann–Mauguin notation, V is the cell volume, and Z corresponds to the number of formula units per unit cell. The relative difference in the unit cell volume V between calculations and experiments, $\Delta V/V = (V_{DFT} - V_{exp})/V_{exp}$, is reported in the last column

Structure	a (Å)	b (Å)	c (Å)	α (°)	β (°)	γ (°)	V (Å^3)	SG	Z	Ref.	$\Delta V/V$
Rubrene polymorphs											
RO	7.17	14.21	26.78	90.0	90.00	90.0	2729.6	*Cmca*	4	Exp.[40]	—
	7.15	14.02	26.45	90.0	90.00	90.0	2653.3			DFT	−0.02
RT	7.01	8.54	11.94	93.0	105.50	96.2	683.5	$P\bar{1}$	1	Exp.[43]	—
	6.93	8.33	11.86	93.0	105.19	96.2	646.2			DFT	−0.05
RM	8.73	10.12	15.63	90.0	90.98	90.0	1383.3	*P*21/*c*	2	Exp.[43]	—
	8.54	9.90	15.49	90.0	90.95	90.0	1310.4			DFT	−0.05
BTBT derivatives											
B0	5.89	8.10	11.90	90.0	106.40	90.0	545.2	*P*21/*c*	2	Exp.[55]	—
	5.80	7.68	11.72	90.0	106.40	90.0	520.3			DFT	−0.04
B8	5.92	7.88	29.18	90.0	92.40	90.0	1362.0	*P*21/*a*	2	Exp.[59]	—
	5.77	7.45	29.12	90.0	92.38	90.0	1251.8			DFT	−0.08
B12	5.86	7.74	37.91	90.0	90.60	90.0	1721.0	*P*21/*a*	2	Exp.[54]	—
	5.73	7.37	38.09	90.0	90.57	90.0	1601.5			DFT	−0.07

Table 2 Transfer integral (J) and hole effective mass (m_h, in units of electron mass) along the crystallographic directions corresponding to the inter-neighbour vector (given in the basis of direct lattice vectors) in rubrene polymorphs and BTBT derivatives

Structure	Direction	J (meV)	m_h	Structure	J (meV)	m_h	Nomenclature	
RO	[100]	107.42	0.67	B0	64.82	1.03	J_1	m_1
	[0.5, 0.5, 0]	20.33	1.05		18.02	2.31	J_2	m_2
	[010]	0.65	2.03		0.78	4.96	J_3	m_3
	[001]	0.35	7.54		0.01	9.54	J_4	m_4
RT	[100]	84.21	0.89	B8	64.49	0.88	J_1	m_1
	[0.5, 0.5, 0]	—	—		69.86	1.09	J_2	m_2
	[010]	11.77	3.15		1.63	4.61	J_3	m_3
	[001]	0.33	8.01		0.3	∞	J_4	m_4
RM	[100]	12.67	3.10	B12	65.41	0.86	J_1	m_1
	[0.5, 0.5, 0]	—	—		69.86	1.09	J_2	m_2
	[010]	5.34	4.91		1.78	4.45	J_3	m_3
	[001]	5.03	4.95		0.00	∞	J_4	m_4

directions **k**, represented by the inter-neighbour vector (see Table 2), and the effective mass was calculated by taking the second derivative of the polynomial. Band structures of all investigated systems are provided in the ESI.†

3 Results and discussion

3.1 Structural and charge transport properties in the absence of strain

Although most investigations on crystalline rubrene concentrated on the orthorhombic form,[9,10,39–42] two additional polymorphs were reported, namely the triclinic[43,44] and monoclinic[45,46] phases. While the base-centered orthorhombic phase is in general obtained from vapor deposition, triclinic and monoclinic phases are obtained from precipitation or reprecipitation methods.[45] It has also been demonstrated that both the rate of precipitation and the type of solvent employed modulate the shape of micro-crystals of triclinic and monoclinic rubrene structures.[45,47] The spatial arrangement of different polymorphs of rubrene are shown in Fig. 1, while the crystallographic parameters are displayed in Table 1. The triclinic phase exhibits a face-to-face slip stack arrangement between the two neighbouring tetracene cores, with an intermolecular distance between the aromatic planes of about 7 Å, similar to that of the orthorhombic phase.[44] However, hole mobilities of the triclinic phase were reported to be lower than those of the orthorhombic one.[44] This decrease in mobility was attributed to the absence of a herringbone disposition of the molecules, and to the lower density of molecular packing along the c-axis, which is perpendicular to the π-stacking direction.[43–45] In contrast to the triclinic and orthorhombic phases, the monoclinic polymorph exhibits minimal π-stacking interactions, leading to a further decrease in mobility.[45]

Thienoacene-based derivatives constitute another class of efficient p-type organic semiconductors, which exhibit high mobility with relatively high air stability, owing to their delocalized electronic structure and deep-lying highest occupied molecular orbitals (HOMOs).[48] In addition, strong non-bonded interactions between sulfur atoms (S–S) and intermolecular π–π interactions in the solid state promote large orbital overlap between the constitutive units.[49] Of particular relevance in the thienoacene family is the [1]benzothieno[3,2-*b*][1]benzothiophene (BTBT) core, from which several derivatives were synthesized.[50–54] BTBT and alkylated derivatives (C_n-BTBT) have been the subject of a series of experimental[55] and computational[56–58] studies, which evidenced an increase in the hole mobilities as a function of n. In the present study, we consider C_n-BTBT derivatives with n equal to zero (B0), eight (B8) and twelve (B12). The spatial arrangement of these materials is presented in Fig. 2, and the crystallographic parameters are gathered in Table 1. For all derivatives, earlier reports have shown that the maximum hole mobility is along the π-stacking direction, which corresponds to the a-axis of the crystal structure.[56–58] Crystallographic parameters of rubrene polymorphs and BTBT derivatives obtained from strain-free PW-DFT relaxations (Table 1) are in fair agreement with the experimental data with a maximum volume deviation of 8%

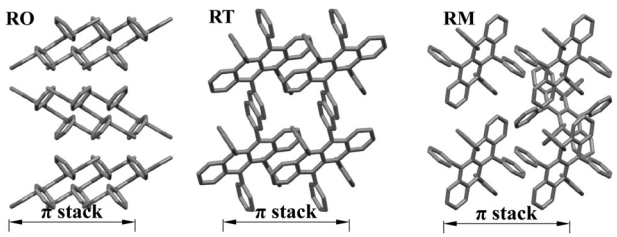

Fig. 1 Crystalline packing of rubrene polymorphs: orthorhombic (RO), triclinic (RT) and monoclinic (RM), viewed along the *ab* plane (π-stacked direction is along the *a* axis). Similarity between the π-stacked arrangements in the orthorhombic and triclinic phases can be noticed. For the sake of clarity, hydrogen atoms are not shown.

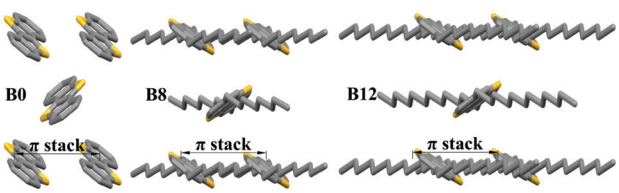

Fig. 2 Crystalline packing of BTBT derivatives: BTBT (B0), C_8-BTBT (B8), and C_{12}-BTBT (B12), viewed along the *ab* plane (π-stacked direction is along the *a* axis). For the sake of clarity, hydrogen atoms are not shown.

obtained for the B8 compound. Complementary assessments of the conductivity of the target materials were performed by calculating effective masses and transfer integral values, both gathered in Table 2. Overall, the results for these two quantities are consistent, *i.e.* the directions along which transfer integrals are large correspond to those along which effective masses are small, in agreement with the theoretical expectation that transfer integrals and effective masses are inversely proportional, although a direct comparison is not possible since effective masses arise for a direction-dependent linear combination of transfer integrals.[60]

In line with previous studies,[12,61] the largest (lowest) transfer integrals (effective masses) in the orthorhombic structure of rubrene are obtained along the π-stacking direction, while electronic couplings are 5 times smaller along the herringbone direction. Similarly, the π-stacking direction in triclinic rubrene gives rise to the largest transfer integral (J_1), while couplings along the *b*-axis are 8 times weaker. The order of magnitude of transfer integrals in monoclinic rubrene is much smaller compared to those calculated in the orthorhombic and triclinic polymorphs. However, the electronic couplings are also more homogeneous, thus imparting to hole transport in the monoclinic phase a more isotropic character than in the orthorhombic and triclinic ones, for which two-dimensional transport properties are instead expected. Similarly, in agreement with previous reports,[56–58,61] C_8-BTBT and C_{12}-BTBT are predicted to exhibit a two-dimensional hole transport with $J_1 \simeq J_2$, while BTBT shows a lower transport dimensionality, with $J_1 > J_2$.

3.2 Mechanical properties

Within the elastic limit of the material, normal stress (σ) and strain (ε) are related by the stiffness tensor, following:

$$\sigma_i = \sum_j C_{ij}\varepsilon_j \qquad (2)$$

where *i* and *j* are any of the three Cartesian axis directions. For simplicity, we aligned the crystal *a*-axis with the Cartesian *x*-axis, and we labeled in the following *b* and *c* the *y* and *z* axes, even if a perfect coincidence of the three directions is possible only for an orthorhombic cell. The stiffness tensor elements were computed by performing a linear regression of the stress–strain plot, imposing an intercept at (0,0). Results, in units of GPa, obtained for rubrene polymorphs and BTBT derivatives are given below:

$$C_{RO} = \begin{bmatrix} 19.5 & 12.4 & 6.6 \\ 12.4 & 15.1 & 6.2 \\ 6.6 & 6.2 & 26.5 \end{bmatrix} \quad C_{B0} = \begin{bmatrix} 19.6 & 12.9 & 5.0 \\ 12.9 & 16.2 & 3.9 \\ 5.0 & 3.9 & 44.3 \end{bmatrix}$$

$$C_{RT} = \begin{bmatrix} 16.9 & 10.5 & 10.1 \\ 10.5 & 17.0 & 11.5 \\ 10.1 & 11.5 & 28.7 \end{bmatrix} \quad C_{B8} = \begin{bmatrix} 17.6 & 9.5 & 12.5 \\ 9.5 & 15.2 & 6.7 \\ 12.5 & 6.7 & 49.3 \end{bmatrix}$$

$$C_{RM} = \begin{bmatrix} 16.7 & 9.8 & 11.3 \\ 9.8 & 14.4 & 12.9 \\ 11.3 & 12.9 & 20.9 \end{bmatrix} \quad C_{B12} = \begin{bmatrix} 16.8 & 8.2 & 13.8 \\ 8.19 & 14.9 & 8.3 \\ 13.8 & 8.3 & 50.9 \end{bmatrix}$$

Poisson ratios and Young's moduli of rubrene polymorphs and BTBT derivatives, computed following the procedure from ref. 12, are reported in Table 3. At first sight, the stiffness matrix elements obtained for rubrene polymorphs show small deviations. However, when focusing on the off-diagonal components, an increase in the stiffness elements C_{ac} and C_{bc} is observed, while C_{ab} decreases, moving from orthorhombic to triclinic and monoclinic. These variations, albeit being sometimes subtle, impact the Poisson ratios of rubrene polymorphs. As reported in Table 3, orthorhombic and triclinic phases of rubrene exhibit the largest ν_{ab} and ν_{ba} values indicating strong mechanical coupling between the *a* and *b* crystal axes, whereas monoclinic rubrene shows larger coupling between the *b* and *c* crystal axes. Similarly, stiffness elements C_{ac} and C_{bc} increase from B0 to B8 and B12, while C_{ab} decreases. All BTBT derivatives also show higher values of ν_{ab} and ν_{ba}, with B8 and B12 exhibiting an additional mechanical coupling between the *a* and *c* crystal axes, with a higher value of ν_{ac}. This strong mechanical coupling between different crystallographic axes is bound to influence the strain–mobility response[12] such that a bi-directional strain mobility response is expected for all materials, *i.e.*, strain induced mobility along any crystallographic direction is expected for mechanical perturbation applied either along the same direction or along any other coupled direction. Further, the Young's moduli of rubrene

Table 3 Elastic constant (E_i, in GPa) of rubrene polymorphs and BTBT derivatives and Poisson ratio (ν_{ij}). The values for orthorhombic rubrene computed in this work are in broad agreement with the literature results, reported in the last three columns

Constants	RO	RT	RM	B0	B8	B12	RO_{DFT}[62]	RO_{EXP}[10]	RO_{MD}[12]
ν_{ba}	0.79	0.52	0.43	0.78	0.54	0.44	0.71	0.60	0.87
ν_{ab}	0.60	0.48	0.26	0.65	0.54	0.45	0.57	0.51	0.49
ν_{ac}	0.16	0.28	0.25	0.20	0.74	0.76	0.20	−0.16	−0.12
ν_{ca}	0.06	0.14	0.26	0.04	0.17	0.20	0.08	−0.10	−0.09
ν_{bc}	0.28	0.49	0.72	0.07	0.00	0.14	0.33	0.62	0.48
ν_{cb}	0.08	0.23	0.47	0.01	0.00	0.01	0.11	0.34	0.21
E_a	9.21	9.98	9.35	9.24	10.1	10.4	8.89	9.01	8.92
E_b	7.04	9.27	5.68	7.7	10.1	10.8	7.14	7.07	5.12
E_c	23.6	20.1	8.71	43.0	40.1	39.3	21.7	14.1	11.9

show small variations from one polymorph to another, which is also the case for BTBT derivatives. Both rubrene polymorphs and BTBT derivatives show comparatively large Young's moduli along the *c*-axis, reflecting that the materials are more elastic along the *c*-axis, which corresponds to the direction along which the inter-molecular distance is the largest. Also, it is interesting to notice the higher values of E_c and C_{cc} for BTBT derivatives with respect to rubrene, suggesting that in BTBTs, despite the presence of "soft" alkyl chain lamellae along the *c*-direction, the fluctuations of molecular positions in and out of the *ab*-plane should be smaller than the ones experienced by rubrene molecules.

3.3 Strain–mobility response from band transport models

In the framework of the semi-classical Drude model, the band mobility (μ) as a function of effective mass (m) can be computed through the following relation:[61,63,64]

$$\mu_j = \frac{e\tau}{m_j} \tag{3}$$

where e is the elementary charge and τ is the relaxation time. Since we are interested in the relative variation of mobility ($\Delta\mu$) along the direction j as a function of applied strain along i, assuming constant electron–phonon coupling, we obtain:

$$\Delta\mu_j^i = \frac{\mu_j^{\varepsilon_i} - \mu_j^0}{\mu_j^0} \approx \frac{m_j^0}{m_j^{\varepsilon_i}} - 1 \tag{4}$$

where the superscripts 0 and ε_i correspond to values obtained for unstrained and strained crystals along the crystallographic direction i, respectively, whereas effective masses are calculated along a second direction j. The assumptions above do not permit the comparison between results obtained for different directions of applied strain, but they are useful to determine the anisotropy of the mobility at a given strain. The variation of mobility estimated from effective masses for rubrene polymorphs and BTBT derivatives is presented in Fig. 3 and 4. Since all compounds exhibit negligible or low mobility along the *c*-axis,[56–58,65,66] as reflected by the low couplings J_3 and J_4 and effective mass values m_3 and m_4 reported in Table 2, the

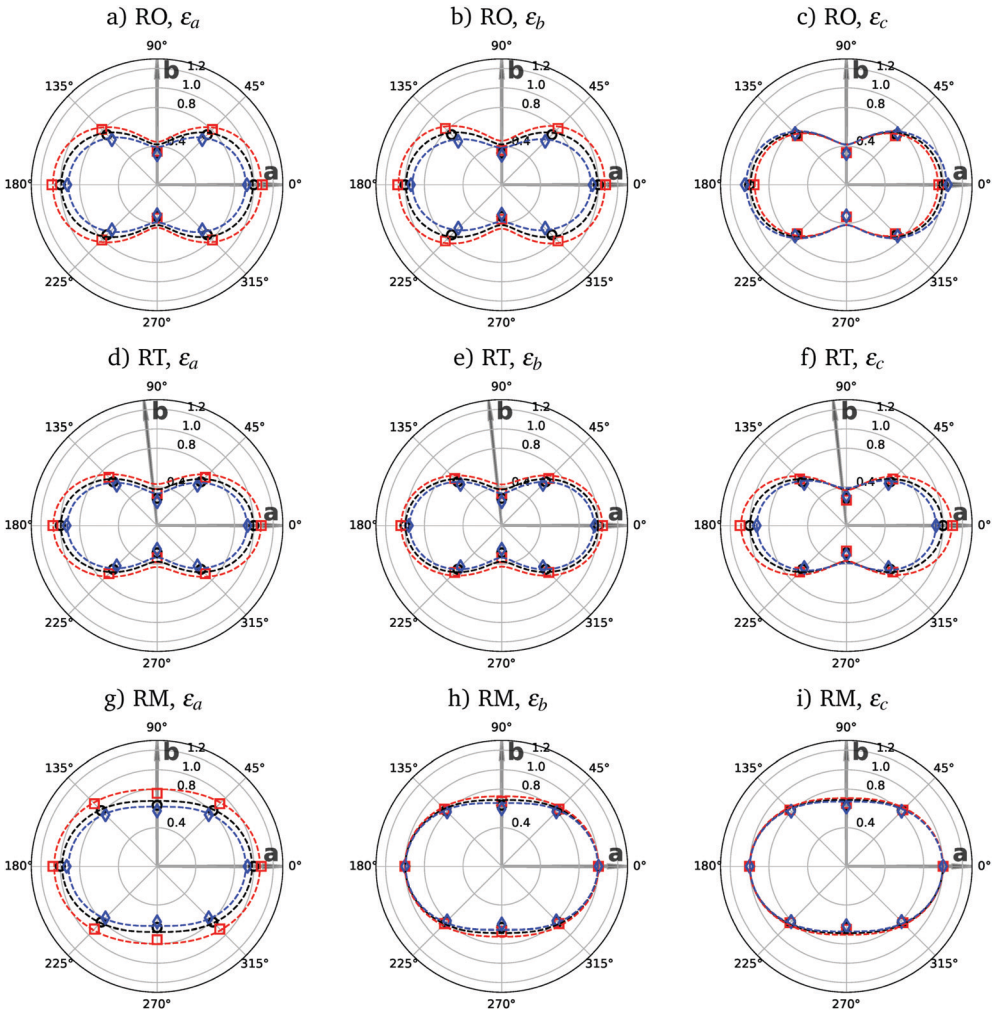

Fig. 3 Polar plot representing the relative mobility variation, $m_j^0 / m_j^{\varepsilon_i}$, in the *ab*-plane (see eqn (3) and (4)) for rubrene polymorphs. Strain is applied along *a* (left panels), *b* (middle), and *c* (right) crystal axes. Black circles correspond to zero strain, red squares correspond to $\varepsilon_i = -0.008$ (compressive), and blue diamonds correspond to $\varepsilon_i = +0.008$ (tensile). Dashed lines correspond to the fit using the function $A_0 + A_1\cos(2x) + A_2\cos(4x)$ and are a guide to the eye.

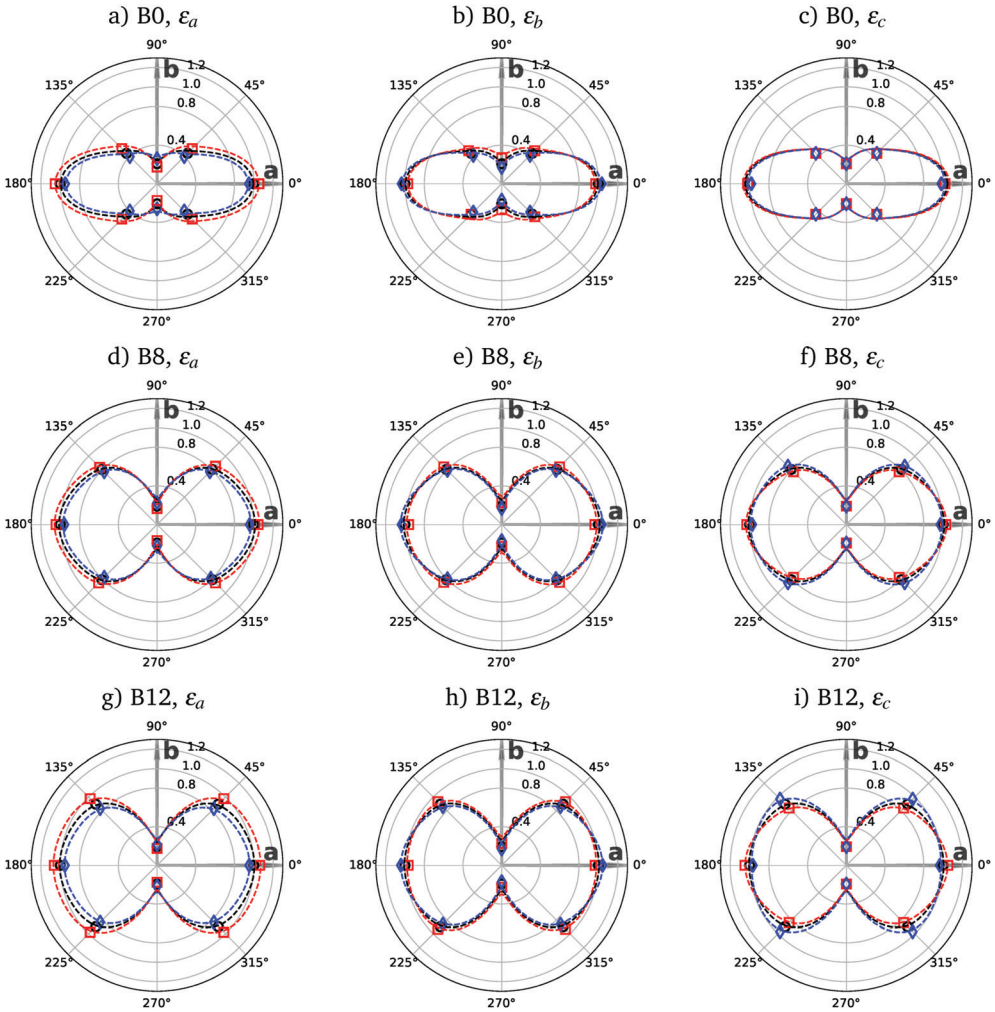

Fig. 4 Polar plot representing the relative mobility variation, $m_j^0 / m_j^{\varepsilon_i}$, in the *ab*-plane (see eqn (3) and (4)) for BTBT derivatives. Strain is applied along *a* (left panels), *b* (middle), and *c* (right) crystal axes. Black circles correspond to zero strain, red squares correspond to $\varepsilon_i = -0.008$ (compressive), and blue diamonds correspond to $\varepsilon_i = +0.008$ (tensile). Dashed lines correspond to the fit using the function $A_0 + A_1\cos(2x) + A_2\cos(4x)$ and are a guide to the eye.

mobility variations and their anisotropy are analyzed only in the *ab* plane, for zero strain and with compressive and tensile strains of 0.8%. The relative changes in effective mass as a function of applied strain, calculated using eqn (4), (reported as percentage change) are also provided in the ESI.†

For all rubrene polymorphs, compressive strains applied along the *a* and *b* axes (Fig. 3a, b, d, e, g and h) produce, as expected, an increase of mobilities in the *ab* plane. Conversely, for strains applied along the *c*-axis, the opposite behaviour is observed for orthorhombic rubrene (Fig. 3c) with mobility slightly increasing upon expansion, whereas the expected standard behaviour is recovered in the triclinic and monoclinic phases (Fig. 3f and i). Actually, the response to strain of the monoclinic phase is negligible for strains applied along *b* and *c*, as clearly shown by the almost superimposed and nearly isotropic curves in Fig. 3h and i.

Similar to the rubrene polymorphs, all BTBT derivatives show an increase in mobility in the *ab*-plane for compressive strains applied along the *a*-axis (Fig. 4a, d and g), while for strains along *b* and *c*, the response in terms of mobility variation appears to be very small (Fig. 4b, c, e, f, h and i), with B8 and B12 derivatives showing slightly larger responses and, for strain along *c*, with mobility increasing upon expansion.

3.4 Strain–mobility response from hopping models

The strain mobility response analysed on the basis of the variation of effective carrier mass in the previous section accounts for the electronic coupling of one molecule with all neighbours in an infinite periodic cell. In other words, the variation of effective mass along the inter-neighbour vector of interest, as a function of strain, is influenced by the presence of other molecules beyond the unit cell. Transfer integrals calculated between isolated pairs of molecules can be employed to isolate this effect. Furthermore, these transfer integrals are fundamental parameters in the hopping theory of charge transport, where the rate is predicted to be dependent on the square of the transfer integral (J^2) itself so that the strain–mobility response can be obtained using eqn (5):[12,65,67]

$$\mu_j^i = \nu \sum_k \left(J_k^i\right)^2 \left(\vec{r}_k^{\,i} \cdot \hat{e}_j\right)^2 \qquad (5)$$

where the summation runs over all the first neighbours k with intermolecular distance vector $\vec{r}_k^i$, $\hat{e}_j$ is a unit vector (in this case, parallel to crystallographic axes), representing the direction along which mobility is measured, and ν is a prefactor containing the details of the transport model.[68] Once mobilities are calculated for different strains with eqn (5), their relative variations can be obtained as in eqn (4).

In the linear response regime, *i.e.*, at low strains, since the squared transfer integral response is approximately linear in the range of strains explored (*vide infra*), a single empirical parameter n_j^i is extracted by using a linear regression to the following equation relating mobility to the applied strain:[13]

$$\mu_j^i = \mu_j^0(1 + n_j^i\varepsilon_i) \quad (6)$$

where j and i indicate again the direction along which the mobility is measured and the direction of applied strain, respectively. The empirical parameter n_j^i contains the relative change of mobility along a specific direction of the crystal, wherein a negative value of n_j^i indicates the standard behaviour in which compressive strains produce an increase in mobility. The values of n_j^i for all systems for $j = (a, b)$ with strain applied along the (a, b, c) axis are reported in Table 4.

All rubrene polymorphs, as well as BTBT derivatives, show an increase in mobility along the a and b axes for compressive strains applied along the a-axis ($n_a^a < 0$ and $n_b^a < 0$), confirming the bi-directional strain–mobility response in these materials. The application of strain along the b-axis (n_j^b) for rubrene polymorphs produces similar effects to the strain along the a-axis, but with a response consistently larger along b than along a. For BTBT derivatives, instead, the response to ε_b is weaker, and its sign is predicted to be negative for the mobility measured along b but positive for measurements along a, as suggested by the corresponding variations of transfer integrals shown in Fig. 8, and in agreement with bandwidth calculations by Shuai and coworkers[69] for B8 derivatives. The situation is even more complex for strain applied along c: while the response for BTBTs is similar but opposite to the one obtained for strains along b, for rubrene polymorphs, there are no clear trends, even though the sign of n_j^c is always different between $j = a$ and $j = b$. Although a recent investigation suggested that mechanical compressive strains of the order of 3% can suppress the intermolecular vibrations, in-turn leading to an increase in mobility,[70] this effect on charge transport properties is not directly addressed in the present work. So, the comparison of the response coefficients reported in Table 4 with experimental ones should be attempted with some caution.

Table 4 Relative strain mobility computed in terms of empirical parameter n_j^i (eqn (6)). A negative (positive) sign of n_j^i indicates an increase (decrease) of mobility on compressive strain. The results for orthorhombic rubrene are in semi-quantitative agreement with the ones in ref. 12

Rubrene polymorphs					BTBT derivatives				
Structure	n_j^i	ε_a	ε_b	ε_c	Structure	n_j^i	ε_a	ε_b	ε_c
RO	μ_a	−8.8	−11.9	+4.2	B0	μ_a	−6.9	+3.7	−0.9
	μ_b	−14.9	−17.6	−5.5		μ_b	−23.3	−7.0	+1.1
RT	μ_a	−13.0	−3.2	−8.2	B8	μ_a	−7.3	+3.0	−2.9
	μ_b	−25.2	−15.1	+4.9		μ_b	−5.9	−3.5	+6.5
RM	μ_a	−14.4	−0.1	+0.1	B12	μ_a	−9.6	+2.2	−3.8
	μ_b	−2.9	−4.4	−1.4		μ_b	−9.7	−5.2	+11.7

3.5 Molecular interpretation of transfer integral variation with strain

To shed light on the origin of mobility variation as a function of mechanical strain, the variations in intra- and intermolecular degrees of freedom caused by the mechanical strain are discussed in conjunction with the resulting transfer integral variations. The relative change in squared transfer integral as a function of strain *via* ΔJ_j^i is given by:

$$\Delta J_j^i = \frac{\left(J_j^{\varepsilon_i}\right)^2 - \left(J_j^0\right)^2}{\left(J_j^0\right)^2} \quad (7)$$

where the subscripts 0 and ε_i correspond to values obtained for unstrained and strained crystals along the crystallographic directions i, and j is the direction along which the transfer integral is calculated. Only transfer integrals for dimers along the highest mobility direction a ([100] in Table 2) are discussed here, while the trends for all other couplings are reported in the ESI.† For compressive (tensile) strains applied along the a axis (π-stacking direction), an increase (decrease) in the corresponding transfer integral (J_1, see Table 2 for nomenclature) is observed for both rubrene polymorphs and BTBT derivatives (Fig. 5). This is not surprising, since the inter-molecular distance decreases (increases) with the application of compressive (tensile) strain and it is well established that the transfer integrals evolve exponentially with intermolecular distance. Transfer integral variations are also observed along the same axis, for strains applied along the b- and c-axes. This result is more appealing, since there is no change in inter-molecular distance between the dimers along the a-axis for strains applied along b and c. This indicates that the transfer integral variations are therefore coupled to other structural variations under the influence of mechanical strain.

One such structural variation is investigated here, by considering the angular displacements between adjacent dimers along the π-stacking direction. The angular displacement is calculated by the change in tilt angle, θ_π, representing the obtuse angle formed by the molecular planes and the a-axis

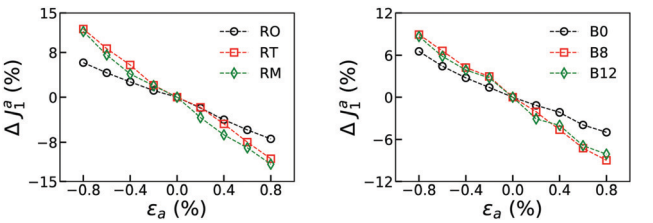

Fig. 5 Relative change in squared transfer integrals for rubrene polymorphs (left) and BTBT derivatives (right) along the π-stacked dimers for strains applied along the π-stacked direction (a-axis).

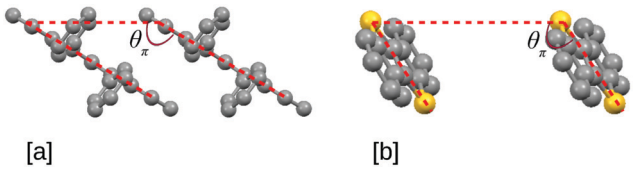

Fig. 6 Definition of the angle θ_π, the main geometrical parameter explaining the effect of applied mechanical strain on transfer integral variations: (a) for rubrene polymorphs and (b) for BTBT derivatives.

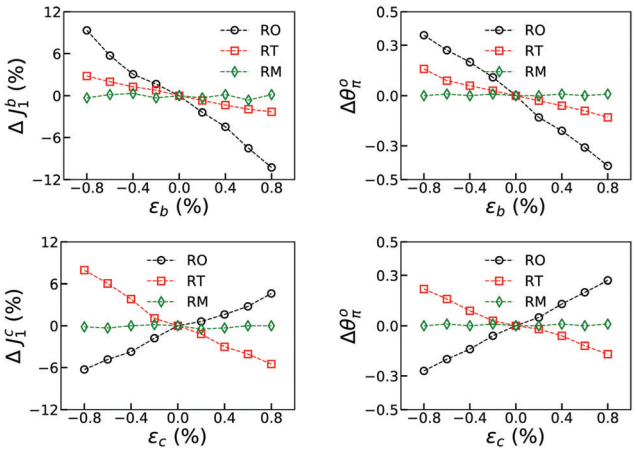

Fig. 7 Relative change in squared transfer integrals and θ_π for rubrene polymorphs along the π-stacked dimers for strains applied along *b* (top) and *c* (bottom) crystallographic directions.

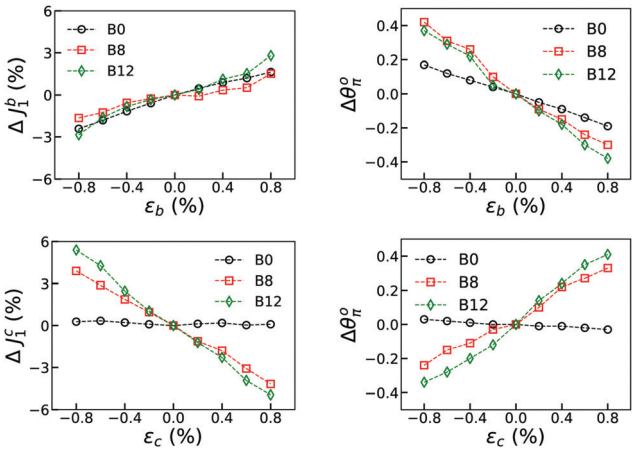

Fig. 8 Relative change in squared transfer integrals and θ_π for BTBT derivatives along the π-stacked dimers for strains applied along *b* (top) and *c* (bottom) crystallographic directions.

(see Fig. 6 for schematic representation). In Fig. 7 and 8, we report the variation of transfer integrals along with the associated change in θ_π, $\Delta\theta_\pi = \theta_\pi^\varepsilon - \theta_\pi^0$, where θ_π^ε and θ_π^0 are the values of θ_π in strain-induced structures and at zero strain, respectively. A similar change in angular displacement of the dimers along the herringbone direction [0.5, 0.5, 0] is also observed. Results related to the variation in transfer integrals associated with the change in herringbone angle are reported in the ESI.† Orthorhombic and triclinic polymorphs of rubrene (Fig. 7) show an increase in θ_π for compressive strains applied along the *b*-axis. This increase in θ_π results in the associated increase of J_1. For compressive strains applied along the *c*-axis, J_1 decreases for orthorhombic rubrene whereas it increases in triclinic rubrene. The relative increase follows the corresponding change in θ_π. Monoclinic rubrene does not show any variation in θ_π for strains applied along the *b*- or *c*-axis, consistent with the weaker mobility variation estimated from effective hole mass (Fig. 3g and i). It follows that for rubrene polymorphs, an increase of θ_π upon strain leads to an increase in the transfer integrals, whereas a decrease in θ_π leads to a decrease in the transfer integrals. Similar to what was observed for rubrene polymorphs, variations in transfer integral J_1 in BTBT derivatives show a strong dependence on θ_π (Fig. 8): compressive strain applied along the *b*-axis leads to an increase in θ_π, which in turn causes the decrease in transfer integrals. For strains applied along the *c*-axis, both B8 and B12 show a similar response, while B0 does not show any response, again in line with the effective mass results (Fig. 4c). However, for strains along the *c*-axis, the direction of change in θ_π and J_1 in BTBT derivatives follows an opposite trend compared to that of the rubrene polymorphs, suggesting that this geometric parameter is indeed relevant but system-dependent in terms of magnitude and direction of the effect.

4 Conclusions

Strain–mobility responses in some high mobility crystalline organic semiconductors, namely three polymorphs of rubrene along with three members from the family of [1]benzothieno[3,2-*b*][1]benzothiophene derivatives, were investigated theoretically. The materials were first characterized in terms of mechanical response, by calculating elastic moduli and Poisson ratios, revealing a higher stiffness of BTBT derivatives, in particular along the direction parallel to the molecular long axes.

The strain mobility response of all materials, calculated using both the band and hopping models of charge transport, shows a bi-directional anisotropic character in any of the crystallographic planes considered (*ab*, *ac* or *bc*), *i.e.*, the mobility response is sensitive to the direction of application of compressive (tensile) strain and the direction of measuring/obtaining the mobility. However, all the materials offer resilience to strain induced mobility variations in the direction perpendicular to the principal transport plane (*ab*). The mobility of monoclinic rubrene, which exhibits lower packing densities compared to the rest of the investigated materials, is rather insensitive to strain in the *ac* and *bc* planes.

It was found that the Poisson ratios are informative as they provide an initial guess about which crystallographic axes are mechanically coupled, and they are indicative of the directions along which the coupled strain–mobility responses can be expected. However, Poisson ratios cannot provide the sign and magnitude of the relative variation of mobility, since the response is rather system dependent, both in terms of magnitude and

direction, and is a result of cumulative effects originating from the inherent structural anisotropy and molecular packing of the material. In particular, the packing densities and the organization of the molecules in the two-dimensional herringbone arrangement emerge as important parameters correlating with the strain–mobility response. These warrant further investigations, at both the fundamental and applied levels.

Conflicts of interest

There are no conflicts to declare.

Acknowledgements

This work was partly funded by the French State grant ANR-10-LABX-0042-AMADEus managed by the French National Research Agency under the initiative of excellence IdEx Bordeaux program (reference ANR-10-IDEX-0003-02). Computer time for this study was provided by "Mésocentre de Calcul Intensif Aquitain" computing facilities of the Université de Bordeaux, Université de Pau et des Pays de l'Adour and the computing facilities of the Consortium des Equipements de Calcul Intensif (CECI, http://www.ceci-hpc.be), and particularly those of the Technological Platform on High-Performance Computing, for which we gratefully acknowledge the financial support of the FNRS-FRFC (Conventions No. 2.4.617.07.F and 2.5020.11). The research in Bologna and Mons was also funded through the European Union's Horizon 2020 research and innovation program under Grant Agreement No. 646176 (EXTMOS project). DB and JC are FNRS Research Directors.

Notes and references

1 Y. Qian, X. Zhang, L. Xie, D. Qi, B. K. Chandran, X. Chen and W. Huang, *Adv. Mater.*, 2016, **28**, 9243–9265.
2 H. Wang, X. Ma and Y. Hao, *Adv. Mater. Interfaces*, 2017, **4**, 1600709.
3 G. H. Gelinck, H. E. A. Huitema, E. van Veenendaal, E. Cantatore, L. Schrijnemakers, J. B. P. H. van der Putten, T. C. T. Geuns, M. Beenhakkers, J. B. Giesbers, B. H. Huisman, E. J. Meijer, E. M. Benito, F. J. Touwslager, A. W. Marsman, B. J. E. van Rens and D. M. de Leeuw, *Nat. Mater.*, 2004, **3**, 106.
4 M. Berggren, D. Nilsson and N. D. Robinson, *Nat. Mater.*, 2007, **6**, 3.
5 S. Lai, I. Temiño, T. Cramer, F. G. del Pozo, B. Fraboni, P. Cosseddu, A. Bonfiglio and M. Mas-Torrent, *Adv. Electron. Mater.*, 2018, **4**, 1700271.
6 T. Someya, Z. Bao and G. G. Malliaras, *Nature*, 2016, **540**, 379–385.
7 T. Q. Trung and N.-E. Lee, *Adv. Mater.*, 2017, **29**, 1603167.
8 A. Chortos and Z. Bao, *Mater. Today*, 2014, **17**, 321–331.
9 A. L. Briseno, R. J. Tseng, M. M. Ling, E. H. L. Falcao, Y. Yang, F. Wudl and Z. Bao, *Adv. Mater.*, 2006, **18**, 2320–2324.
10 M. A. Reyes-Martinez, J. A. Crosby and A. L. Briseno, *Nat. Commun.*, 2015, **6**, 6948.
11 T. Morf, T. Mathis and B. Batlogg, 2016, arXiv:1606.06875v2.
12 M. Matta, M. J. Pereira, S. M. Gali, D. Thuau, Y. Olivier, A. L. Briseno, I. Dufour, C. Ayela, G. Wantz and L. Muccioli, *Mater. Horiz.*, 2018, **5**, 41–50.
13 P. Heremans, A. K. Tripathi, A. de Jamblinne de Meux, E. C. P. Smits, B. Hou, G. Pourtois and G. H. Gelinck, *Adv. Mater.*, 2016, **28**, 4266–4282.
14 Y. Esaki, T. Matsushima and C. Adachi, *Adv. Funct. Mater.*, 2016, **26**, 2940–2949.
15 Z. Rang, M. I. Nathan, P. P. Ruden, V. Podzorov, M. E. Gershenson, C. R. Newman and C. D. Frisbie, *Appl. Phys. Lett.*, 2005, **86**, 1–3.
16 M. Oehzelt, A. Aichholzer, R. Resel, G. Heimel, E. Venuti and R. G. Della Valle, *Phys. Rev. B: Condens. Matter Mater. Phys.*, 2006, **74**, 1–7.
17 A. Jedaa and M. Halik, *Appl. Phys. Lett.*, 2009, **95**, 103309.
18 A. N. Sokolov, Y. Cao, O. B. Johnson and Z. Bao, *Adv. Funct. Mater.*, 2012, **22**, 175–183.
19 G. Giri, E. Verploegen, S. Mannsfeld, S. Atahan-Evrenk, D. H. Kim, S. Y. Lee, H. A. Becerril, A. Aspuru-Guzik, M. F. Toney and Z. Bao, *Nature*, 2011, **480**, 504–508.
20 K. Sakai, Y. Okada, S. Kitaoka, J. Tsurumi, Y. Ohishi, A. Fujiwara, K. Takimiya and J. Takeya, *Phys. Rev. Lett.*, 2013, **110**, 1–5.
21 H. T. Yi, M. M. Payne, J. E. Anthony and V. Podzorov, *Nat. Commun.*, 2012, **3**, 1259.
22 V. Raghuwanshi, D. Bharti and S.-P. Tiwari, *Org. Electron.*, 2016, **31**, 177–182.
23 X. Zheng, H. Geng, Y. Yi, Q. Li, Y. Jiang, D. Wang and Z. Shuai, *Adv. Funct. Mater.*, 2014, **24**, 5531–5540.
24 Y. Park, K. S. Park, B. Jun, Y.-E. K. Lee, S. U. Lee and M. M. Sung, *Chem. Mater.*, 2017, **29**, 4072–4079.
25 Y. Wu, A. Chew, G. Rojas, G. Sini, G. Haugstad, A. Belianinov, S. V. Kalinin, H. Li, C. Risko, J.-L. Brédas, A. Salleo and C. D. Frisbie, *Nat. Commun.*, 2016, **7**, 10270.
26 T. Cramer, L. Travaglini, S. Lai, L. Patruno, S. de Miranda, A. Bonfiglio, P. Cosseddu and B. Fraboni, *Sci. Rep.*, 2016, **6**, 38203.
27 Y. Mei, P. J. Diemer, M. R. Niazi, R. K. Hallani, K. Jarolimek, C. S. Day, C. Risko, J. E. Anthony, A. Amassian and O. D. Jurchescu, *Proc. Natl. Acad. Sci. U. S. A.*, 2017, **114**, E6739–E6748.
28 M. J. Pereira, M. Matta, L. Hirsch, I. Dufour, A. Briseno, S. M. Gali, Y. Olivier, L. Muccioli, A. Crosby, C. Ayela and G. Wantz, *ACS Appl. Mater. Interfaces*, 2018, **10**, 41570–41577.
29 P. Giannozzi, S. Baroni, N. Bonini, M. Calandra, R. Car, C. Cavazzoni, D. Ceresoli, G. L. Chiarotti, M. Cococcioni, I. Dabo, A. Dal Corso, S. de Gironcoli, S. Fabris, G. Fratesi, R. Gebauer, U. Gerstmann, C. Gougoussis, A. Kokalj, M. Lazzeri, L. Martin-Samos, N. Marzari, F. Mauri, R. Mazzarello, S. Paolini, A. Pasquarello, L. Paulatto, C. Sbraccia, S. Scandolo, G. Sclauzero, A. P. Seitsonen, A. Smogunov, P. Umari and R. M. Wentzcovitch, *J. Phys.: Condens. Mater.*, 2009, **21**, 395502.

30 T. Thonhauser, V. R. Cooper, S. Li, A. Puzder, P. Hyldgaard and D. C. Langreth, *Phys. Rev. B: Condens. Matter Mater. Phys.*, 2007, **76**, 125112.
31 R. Sabatini, E. Küçükbenli, B. Kolb, T. Thonhauser and S. D. Gironcoli, *J. Phys.: Condens. Matter*, 2012, **24**, 424209.
32 T. Thonhauser, S. Zuluaga, C. A. Arter, K. Berland, E. Schröder and P. Hyldgaard, *Phys. Rev. Lett.*, 2015, **115**, 136402.
33 V. R. Cooper, *Phys. Rev. B: Condens. Matter Mater. Phys.*, 2010, **81**, 161104.
34 K. Berland and P. Hyldgaard, *Phys. Rev. B: Condens. Matter Mater. Phys.*, 2014, **89**, 035412.
35 K. Berland, V. R. Cooper, K. Lee, E. Schröder, T. Thonhauser, P. Hyldgaard and B. I. Lundqvist, *Rep. Prog. Phys.*, 2015, **78**, 066501.
36 E. F. Valeev, V. Coropceanu, A. D. da Silva Filho, S. Salman and J.-L. Brédas, *J. Am. Chem. Soc.*, 2006, **128**, 9882–9886.
37 G. te Velde, F. M. Bickelhaupt, E. J. Baerends, C. Fonseca Guerra, S. J. A. van Gisbergen, J. G. Snijders and T. Ziegler, *J. Comput. Chem.*, 2001, **22**, 931–967.
38 G. A. de Wijs, C. C. Mattheus, R. A. de Groot and T. T. M. Palstra, *Synth. Met.*, 2003, **139**, 109–114.
39 D. Käfer and G. Witte, *Phys. Chem. Chem. Phys.*, 2005, **7**, 2850.
40 M. El Helou, O. Medenbach and G. Witte, *Cryst. Growth Des.*, 2010, **10**, 3496–3501.
41 E. Menard, V. Podzorov, S. H. Hur, A. Gaur, M. E. Gershenson and J. A. Rogers, *Adv. Mater.*, 2004, **16**, 2097–2101.
42 M. A. Reyes-Martinez, A. Ramasubramaniam, A. L. Briseno and A. J. Crosby, *Adv. Mater.*, 2012, **24**, 5548–5552.
43 L. Huang, Q. Liao, Q. Shi, H. Fu, J. Ma and J. Yao, *J. Mater. Chem.*, 2010, **20**, 159–166.
44 M. Takeshi, Y. Masashi, U. Masahito, Y. Masakazu, N. Akiko, T. Yoshinori, T. Junichi, K. Yasuo, M. Yusuke and S. Takatomo, *Jpn. J. Appl. Phys.*, 2010, **49**, 085502.
45 S. Bergantin and M. Moret, *Cryst. Growth Des.*, 2012, **12**, 6035–6041.
46 T. Salzillo, R. G. D. Valle, E. Venuti, A. Brillante, T. Siegrist, M. Masino, F. Mezzadri and A. Girlando, *J. Phys. Chem. C*, 2016, **120**, 1831–1840.
47 X. Wang, Y. Garcia, S. Monaco and A. N. M. B. Schatschneider, *CrystEngComm*, 2016, **18**, 7353–7362.
48 C. Wang, H. Dong, W. Hu, Y. Liu and D. Zhu, *Chem. Rev.*, 2012, **112**, 2208–2267.
49 J. Huang, H. Luo, L. Wang, Y. Guo, W. Zhang, H. Chen, M. Zhu, Y. Liu and G. Yu, *Org. Lett.*, 2012, **14**, 3300–3303.
50 B. Košata, V. Kozmik, J. Svoboda, V. Novotná, P. Vaněk and M. Glogarová, *Liq. Cryst.*, 2003, **30**, 603–610.
51 K. Bedřich, S. Jiří, N. Vladimíra and G. Milada, *Liq. Cryst.*, 2004, **31**, 1367–1380.
52 K. Takimiya, H. Ebata, K. Sakamoto, T. Izawa, T. Otsubo and Y. Kunugi, *J. Am. Chem. Soc.*, 2006, **128**, 12604–12605.
53 K. Takimiya, S. Shinamura, I. Osaka and E. Miyazaki, *Adv. Mater.*, 2011, **23**, 4347–4370.
54 H. Ebata, T. Izawa, E. Miyazaki, K. Takimiya, M. Ikeda, H. Kuwabara and T. Yui, *J. Am. Chem. Soc.*, 2007, **129**, 15732–15733.
55 K. Takimiya, I. Osaka, T. Mori and M. Nakano, *Acc. Chem. Res.*, 2014, **47**, 1493–1502.
56 C. Niebel, Y. Kim, C. Ruzie, J. Karpinska, B. Chattopadhyay, G. Schweicher, A. Richard, V. Lemaur, Y. Olivier, J. Cornil, A. R. Kennedy, Y. Diao, W.-Y. Lee, S. Mannsfeld, Z. Bao and Y. H. Geerts, *J. Mater. Chem. C*, 2015, **3**, 674–685.
57 C. Ruzie, J. Karpinska, A. Laurent, L. Sanguinet, S. Hunter, T. D. Anthopoulos, V. Lemaur, J. Cornil, A. R. Kennedy, O. Fenwick, P. Samorì, G. Schweicher, B. Chattopadhyay and Y. H. Geerts, *J. Mater. Chem. C*, 2016, **4**, 4863–4879.
58 Y. Tsutsui, G. Schweicher, B. Chattopadhyay, T. Sakurai, J.-B. Arlin, C. Ruzié, A. Aliev, A. Ciesielski, S. Colella, A. R. Kennedy, V. Lemaur, Y. Olivier, R. Hadji, L. Sanguinet, F. Castet, S. Osella, D. Dudenko, D. Beljonne, J. Cornil, P. Samor, S. Seki and Y. H. Geerts, *Adv. Mater.*, 2016, **28**, 7106–7114.
59 I. Izawa, E. Miyazaki and K. Takimiya, *Adv. Mater.*, 2008, **20**, 3388–3392.
60 K. Hannewald, V. M. Stojanović, J. M. T. Schellekens, P. A. Bobbert, G. Kresse and J. Hafner, *Phys. Rev. B: Condens. Matter Mater. Phys.*, 2004, **69**, 075211.
61 K. Kobayashi, K. Norihito, H. Shizuka, K. Naoki, M. Daisuke, S. Raku, K. Yoshihiro, H. Daisuke, T. Yuichi and I. Masao, *J. Chem. Phys.*, 2013, **139**, 014707.
62 Y. Zhang, D. Manke, S. Sharifzadeh, A. Briseno, A. Ramasubramaniam and K. Koski, *Appl. Phys. Lett.*, 2017, **110**, 071903.
63 N. Bannov, V. Aristov, V. Mitin and M. Stroscio, *Phys. Rev. B: Condens. Matter Mater. Phys.*, 1995, **51**, 9930–9942.
64 S. Fratini, D. Mayou and S. Ciuchi, *Adv. Funct. Mater.*, 2016, **26**, 2292–2315.
65 V. Stehr, J. Pfister, R. Fink, B. Engels and C. Deibel, *Phys. Rev. B: Condens. Matter Mater. Phys.*, 2011, **83**, 155208.
66 V. Stehr, R. F. Fink, M. Tafipolski, C. Deibel and B. Engels, *Wiley Interdiscip. Rev.: Comput. Mol. Sci.*, 2016, **6**, 694–720.
67 W.-G. Deng and W. A. Goddard III, *J. Phys. Chem. B*, 2004, **108**, 8614–8621.
68 V. Coropceanu, J. Cornil, D. A. da Silva Filho, Y. Olivier, R. Silbey and J.-L. Brédas, *Chem. Rev.*, 2007, **107**, 926–952.
69 J. Chen, W. Shi, Y. Jiang, D. Wang and Z. Shuai, *Sci. China: Chem.*, 2017, **60**, 275–283.
70 T. Kubo, R. Häusermann, J. Tsurumi, J. Soeda, Y. Okada, Y. Yamashita, N. Akamatsu, A. Shishido, C. Mitsui, T. Okamoto, S. Yanagisawa, H. Matsui and J. Takeya, *Nat. Commun.*, 2016, **7**, 11156.